HiSST: 3rd International Conference on
High-Speed Vehicle Science Technology

14–19 April 2024, Busan, Korea

Numerical Study on Post-Combustion Chamber Impact on Hybrid Rocket Performance

A. Dabanović[1], J. Martin[1], S. May[2], V. Wartemann[1]

Abstract

In chemical propulsion, propellant masses are generally the largest part of the overall weight. Hence, combustion efficiency is a key aspect of the system's performance and small improvements within the combustion process can result in significant changes in project costs or mission longevity. To analyze detailed chemical and physical processes, direct measurements are cost-intensive and limited to lab-scale devices. Numerical investigations have therefore become a widely used tool to simulate the inner flow and combustion of propulsion systems. In hybrid rocket engines, post-combustion chambers are used to improve the mixing and combustion process. Nevertheless, these components imply additional structural mass and engine length. This study analyzes the influence of different post-combustion chamber lengths on the combustion efficiency. The simulations were performed in two-dimensional, axisymmetric domains with fuel mass flow and detailed combustion modeling. The efficiency is shown to increase linearly with increasing post-chamber length. However, it is significantly influenced by turbulator components. With these results, the qualitative influence of post-combustion chambers is analyzed, enabling optimization of engine design while ensuring sufficient combustion efficiency.

Keywords: *hybrid rocket propulsion, computational fluid dynamics, post-combustion chamber design, numerical performance analysis, combustion modelling*

Nomenclature

Abbreviations

CFD	Computational fluid dynamics
DLR	German Aerospace Center
HRM	Hybrid rocket motor
HTPB	Hydroxyl-terminated polybutadiene
LFI	Low frequency instability
RANS	Reynolds-averaged Navier Stokes
SRM	Solid rocket motor

Latin

A	Area
c^*	Characteristic velocity
C_F	Thrust coefficient
F	Thrust
H	Enthalpy
m	Mass
$\dot{m}$	Mass flow
p	Pressure
R	Gas constant
T	Temperature
M	Mach number
t	Time

Greek

ϵ	Nozzle expansion area ratio
κ	Specific heat ratio
Γ	Vandenkerckhoven function
η	Efficiency
ρ	Density

Subscripts

a	Ambient
c	Combustion, Combustion chamber
e	Exit
id	Ideal
pcc	Post-combustion chamber
s	Specific
t	Nozzle throat
w	Wall

[1]*German Aerospace Center (DLR), Institute of Aerodynamics and Flow Technology, Department Spacecraft, Lilienthalplatz 7, 38108 Braunschweig, Germany, andrija.dabanovic@dlr.de, joel.martin@dlr.de, viola.wartemann@dlr.de*

[2]*German Aerospace Center (DLR), Responsive Space Cluster Competence Center (RSC³), Launch Segment, Lilienthalplatz 7, 38108 Braunschweig, Germany, stefan.may@dlr.de*

1. Introduction

Since 2009, the German Aerospace Center (DLR) is developing the AHRES software for the preliminary design of hybrid and solid rocket engines [1]. To validate the calculations, test firings are performed at DLR-site Trauen and numerical simulations are conducted with the DLR TAU-Code [2]. Since common hybrid rocket motors (HRM) combine a liquid oxidizer and solid fuel, they inherit advantages of both liquid and solid rocket motors (SRM). While the spatial separation of the propellants ensures high safety for storage, handling and transportation, the liquid oxidizer potentially enables shutdown, reignition and thrust throttling. Therefore, these engines show higher flexibility and a significant higher safety than solid motors. The fluid system of hybrid motors needs to be designed for only one liquid phase, leading to a simpler architecture and fewer rotary components compared to liquid engines. Subsequently, HRM tend to be more robust and fail-safe. Another key aspect is the variability of propellants leading to non-toxic combinations. Hence, environmental impact can be reduced at ground level as well as high altitudes, where the influence of exhaust gases is strongly increased. Combustion efficiencies of certain propellants, commonly given by the specific impulse, are higher than those of SRM. Nonetheless, liquid rocket efficiencies are not yet reached. All of these aspects decrease developing and operating costs, making hybrid motors a promising alternative to common chemical propulsion systems.

Despite the advantages of hybrid propulsion, its complex combustion process leads to nonlinear behavior when scaling up from laboratory to an operational scale. However, most studies in past and current research where conducted for laboratory scale engines. This is considered as one of the main reasons HRM did not yet reach their full potential and therefore commercial applications [3]. The combustion within the engines is characterized by a diffusion flame with an oxidizer rich core flow and a fuel rich zone within the boundary layer. A detailed understanding of the internal flow dynamics is therefore mandatory to further push the boundaries of current hybrid propulsion limitations, including their scalability. Considering upscaled HRM, the combustion efficiency represents a key aspect due to the high fraction of propellant mass in chemical propulsion systems.

The diffusion flame characteristics cause the flame zone to be more distant to the fuel surface compared to SRM. This leads to a reduced heat transfer and subsequently reduced fuel gasification and fuel mass flow. In the following, this mass flow blocks a certain part of the heat transferred to the surface [4]. The respective low regression rate of HRM is a widely investigated disadvantage. Besides the used solid fuel, especially the fuel geometry is of key importance, since complex geometries can enhance turbulence and therefore heat transfer. Different helical or segmented geometries have been investigated, showing significantly increased fuel regression rates [5, 6]. Since mixing of the reactants within the flow is important to ensure complete combustion, there is a need for detailed analysis of combustion evolution along the engine axis. In this context, unburnt fuel needs to be reduced as much as possible before the mixture exits the engine nozzle. Besides complex fuel geometries, this can be addressed by adding additional components after the combustion chamber, such as turbulator plates and post-combustion chambers. Although post-combustion chambers are suspected to induce low-frequency instabilities (LFI), they are predominantly used to improve mixing of unburnt reactants [7]. Moreover, they decrease the oxidizer mass fractions in the HRM-typical core stream and enhance combustion efficiency. The influence of different chamber lengths is investigated in the following, including efficiency evaluation based on numerical results.

2. Performance Evaluation

Besides the classification of propulsion systems in thrust classes, combustion efficiency is often used to categorize rocket engines. The most comprehensive parameter describing the complete performance is the specific impulse I_{sp}, defined as

$$I_{sp} = \frac{F}{\dot{m}} = C_F \; c^* \tag{1}$$

The first definition of the specific impulse as the ratio of thrust F to nozzle mass flow $\dot{m}$ gives an indication for the overall efficiency of the propulsion system. Assuming ideal processes within the

engine, the I_{sp} is also commonly used to evaluate and compare propellant combinations. As such, this parameter comprises both main processes included in chemical propulsion. First, the transformation of chemical into thermal energy, and second, the transformation of thermal into kinetic energy. In rocket propulsion, two parameters were introduced to directly describe the specific impulse as defined in the second definition of Equation 1. Here, C_F represents the thrust coefficient which is generally defined as the ratio of thrust F to the product of chamber pressure p_c and nozzle throat area A_t:

$$C_F = \frac{F}{p_c \, A_t} \tag{2}$$

Hence, it compares the transformed kinetic energy to the conditions within the combustion chamber and can be interpreted as a nozzle performance parameter. The second parameter is called the characteristic velocity c^*. Combining equations 1 and 2, it can be defined as:

$$c^* = \frac{p_c \, A_t}{\dot{m}} \tag{3}$$

As can be seen, the characteristic velocity compares mass flow and chamber pressure. Therefore, it describes the first process of chemical energy transformation into thermal energy and represents one of the main parameters of this study that focuses on the combustion efficiency. Generally, the chamber pressure p_c represents the global chamber pressure but can be resolved locally in terms of numerical simulations. With the nozzle throat area and the nozzle mass flow being a constant scalar value, local evaluation of the characteristic velocity would directly result in a scaled pressure field of the analysed field domain. Hence, the characteristic velocity is more suitable to compare different propellant compositions as well as to analyze an engine test firing independent of nozzle influence.

Local resolving of the characteristic velocity was conducted by Bendana et al. [8] applying laser absorption spectroscopy. Via measurements of local temperature T and gas composition, the characteristic velocity was determined by

$$c^* = \sqrt{\frac{R_s T}{\kappa} \left(\frac{\kappa+1}{2}\right)^{\frac{\kappa+1}{\kappa-1}}} = \frac{\sqrt{R_s \, T_c}}{\Gamma} \tag{4}$$

with R_s representing the specific gas constant, κ the heat capacity ratio and T_c the chamber temperature. This equation assumes Mach 1 in the nozzle throat, as well as isentropic and therefore adiabatic flow. The parameter Γ represents the Vandenkerckhove function defined as

$$\Gamma = \sqrt{\kappa} \left(\frac{2}{\kappa+1}\right)^{\frac{\kappa+1}{2(\kappa-1)}} \tag{5}$$

However, measurement of local gas composition and temperature is usually conducted in laboratory engines and often limited to a reduced number of species. The resulting field of resolved characteristic velocities does not define the overall combustion efficiency and mainly depends on local flow and vortex formation. Hence, this method is not suitable for the evaluation of CFD-based field solutions.

2.1. Combustion Efficiency

While focussing on the combustion process itself, its efficiency can be defined in different ways that always follow the idea of transformation of chemical energy, stored within the propellants, into thermal energy.

$$\eta_c = \frac{\text{Thermal energy usable for kinetic expansion}}{\text{Chemical energy stored within the propellants}} \tag{6}$$

In terms of the combustion temperature, the efficiency may be defined as the ratio of actual to ideal combustion temperature. This expression is normally derived from thermodynamic cycle processes, assuming ideal gas behavior. While expanding the fraction as shown below, this definition can be transformed into using the characteristic velocity defined in equation 4.

$$\eta_c = \frac{T_c}{T_{c,id}} = \frac{\left(\frac{\sqrt{R_s\ T_c}}{\Gamma}\right)^2}{\left(\frac{\sqrt{R_s\ T_{c,id}}}{\Gamma}\right)^2} = \left(\frac{c^*}{c^*_{id}}\right)^2 \tag{7}$$

Rust et al. [9] analyzed mixing and combustion in the context of supersonic combustion and defined a mixing efficiency of fuel and oxidizer as the ratio of fuel concentration to overall fuel mass flux. Following this, combustion efficiency is defined by means of residual fuel inside the stream. Due to the large vortex formation within the post-combustion chambers, this approach could lead to partially decreasing efficiencies along the engine exit. Similar to this but focussed on chemical reaction advancement, Castiñeira and Edgar [10] defined the combustion efficiency as the ratio of carbon mass flows of produced carbon dioxide as the end product of complete combustion and carbon fuel mass flow.

$$\eta_c = \frac{\dot{m}_C\,(CO_2,\ out)}{\dot{m}_C\,(C_xH_y,\ in)} \tag{8}$$

Assuming the total carbon inflow resulting from fuel pyrolysis, the respective calculation is given by

$$\eta_c = \frac{\frac{M_C}{M_{CO_2}}\ (Y_{CO_2}\ \dot{m})_{out}}{4\frac{M_C}{M_{C_4H_6}}\ (Y_{C_4H_6}\ \dot{m}_f)_{in}} \tag{9}$$

Hence, locally resolved numerical data is used for the evaluation of the combustion efficiency. However, Equation 9 will lead to relatively low values since only complete reactions are considered, while intermediate products do not contribute to the efficiency. Each approach mentioned above refers basically to Equation 6 and illustrates a parameter to evaluate the advancement of combustion processes.

2.2. Variable Evaluation

In the evaluation of the simulation results, every quantity ϕ is integrated along the nozzle exit plane according to

$$\bar{\phi} = \frac{1}{A}\int \phi\, dA \tag{10}$$

Hence, spatially resolved variables are considered, which is the main advantage of numerical tools compared to highly complex and therefore cost-intensive or even unfeasible measurement techniques. For example, engine thrust is calculated via integration of the momentum conservation without gravitation.

$$\sum \vec{F} = \frac{d}{dt}\int_{cv} \rho\vec{v}\, dV + \oint_{cs} \vec{v}\rho(\vec{v}\cdot\vec{n})\, dS + \oint_{cs} p\vec{n}\, dS$$

Assuming steady state conditions as well as symmetric forces in radial and tangential directions, the equation is reduced to the following.

$$F_x = \oint_{cs} v_x^2 \rho \, dS + \oint_{cs} p n_x \, dS \tag{12}$$

This equation subsequently results in the equation for the axial direction on the nozzle exit area:

$$F_x = 2\pi \int_r (r\rho v_x^2 + rp) \, dr - p_a A_e \tag{13}$$

Using this representation, the actual engine thrust derived by the CFD results can be evaluated.

3. Simulation Domain

A generic hybrid rocket engine was designed as the simulation reference within this study. The motor comprises a telescope geometry and produces a nominal thrust of 200 N. Burn time and chamber pressure are set to 10 s and 20 bar respectively, and the fuel block length is 140 mm. The engine uses highly concentrated hydrogen peroxide as oxidizer and hydroxyl-terminated polybutadiene (HTPB) as solid fuel. This propellant combination is widely used and analyzed, also within the AHRES program of the DLR [11]. In the following, the generic engine design, numerical settings and the convergence study are described.

3.1. Generic Engine Design

Thermodynamic properties required for the preliminary design were calculated by the CEA Code (Chemical Equilibrium with Applications) [12]. According to Chiaverini et al. [13], the main pyrolysis product of HTPB can be assumed to be 1,3-butadiene. The oxidizer decomposes catalytically and exothermically to gaseous oxygen and water, according to

$$2H_2O_2 \rightarrow 2H_2O + O_2 + \Delta H \tag{14}$$

Propellant composition and the respective conditions are summarized in Table 1. Mass fractions are calculated according to a concentration of 87.5-wt.% of the hydrogen peroxide. The pyrolysis temperature of HTPB was set according to Reference [14].

Table 1. Propellant composition and boundary temperature

	Parameter	Value	Units
Oxidizer	Mass fraction H_2O	0.58	-
	Mass fraction O_2	0.42	-
	Catalytic temperature	923	K
Fuel	Mass fraction C_4H_6	1.0	-
	Pyrolysis temperature	1050	K

Based on the values mentioned above, the engine parameters are calculated according to the following procedure. The thrust coefficient is determined according to Equation 2 assuming steady and isentropic flow, which leads to

$$C_F = \sqrt{\frac{2\kappa^2}{\kappa - 1} \cdot \left(\frac{2}{\kappa + 1}\right)^{\frac{\kappa+1}{\kappa-1}} \cdot \left[1 - \left(\frac{p_e}{p_c}\right)^{\frac{\kappa-1}{\kappa}}\right]} + \frac{p_e - p_a}{p_c} \cdot \frac{A_e}{A_t} \tag{15}$$

Assuming a well-adapted nozzle and nearly ideal nozzle expansion to ambient pressure, the second term of Equation 15 can be neglected.

The nozzle expansion area ratio is subsequently calculated via

$$\epsilon = \frac{A_e}{A_t} = \frac{\Gamma^2}{\left(\frac{p_e}{p_c}\right)^{\frac{1}{\kappa}} \cdot C_F} \tag{16}$$

Oxidizer and fuel mass flow are determined via the oxidizer-to-fuel (O/F) ratio given by the CEA code for maximum I_{sp} and the total mass flow as a function of desired engine thrust. Combining the Equations 3 and 4, the total mass flow is given by

$$\dot{m}_{total} = \Gamma \cdot \frac{p_c A_t}{\sqrt{R_s T_c}} \tag{17}$$

The fuel geometry is subsequently calculated by assuming a typical and axially constant regression rate and necessary fuel volume for the specified burn time. The calculations described above define most of the engine inner geometry. Additionally, the injector and the post-combustion chamber are designed to provide axial oxidizer inflow and enhanced propellant mixing, respectively. The engine data is summarized in Table 2.

Table 2. Engine design parameters and calculation results

Parameter	Value	Units	Ref.
Fuel regression rate $\dot{r}$	0.5	mm/s	-
Chamber pressure p_c	20.0	bar	-
Specific heat ratio κ	1.135	-	[12]
Thrust coefficient C_F	1.424	-	Eq. 15
Nozzle expansion area ratio ϵ	3.93	-	Eq. 16
Characteristic velocity c^*	1593.27	m/s	[12]
Mixture ratio	6.8	-	[12]
Fuel mass flow $\dot{m}_f$	11.75	g/s	Eq. 17
Oxidizer mass flow $\dot{m}_{ox}$	79.93	g/s	Eq. 17

Several post-combustion chamber lengths ranging from 13 mm to 4 mm with and without a turbulator plate separation towards the combustion chamber are designed. The engine properties described above as well as mesh generation parameters are held constant throughout each simulation.

3.2. Numerical Setup

The DLR TAU-Code uses the Reynolds-averaged Navier-Stokes equations (RANS). For robust modeling of the viscous flow, a single transport equation in the form of the negative Spalart-Allmaras model is used [15]. The model is based on the standard S-A model for compressible flow with minor modifications to avoid negative values of the transport variables to increase numerical stability. This one-equation model allows efficient turbulence modeling and is widely used and verified for different applications [2]. Additional simulations on the reference mesh were conducted using a two-equation model. The Shear-Stress Transport turbulence model presented by Menter [16] is applied here, allowing for more detailed calculations of vortices in the flow domain. It combines the $k-\epsilon$ model, which accurately predicts turbulence behavior in attached freestream-regions, with the $k-\omega$ model, correcting the flow in the inner regions of the boundary layer [17].

The chemically reactive flow is modeled using a reaction rate mechanism. The Westbrook and Dryer multistep mechanism is applied, representing the combustion of 12 species with 22 reactions in total [18]. This simplified mechanism enables analysis of unstable, intermediate combustion products

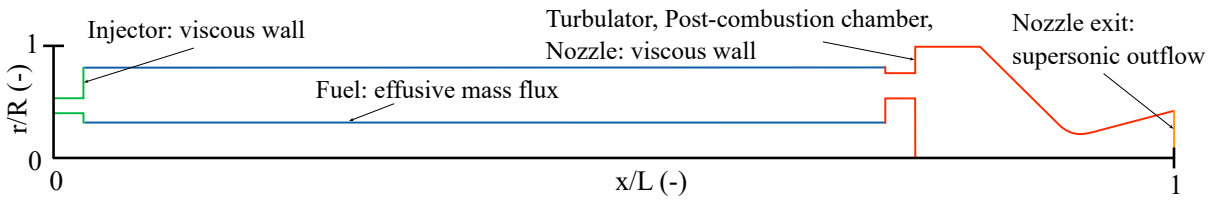

Fig 1. Simulation domain with boundary conditions

Table 3. Total numbers of cells for the mesh convergence study

Mesh	R-1	R-2	R-3	R-4
Number of Cells	205308	262179	293104	320768
Ratio	100.0 %	127.7 %	142.8 %	156.24 %

without introducing an excessive number of reactions to be solved in each numerical iteration. Reaction rates are calculated via a modified Arrhenius-type law.

$$k_r = A_r T^{n_r} \cdot exp\left(\frac{-E_{a,r}}{R_u T}\right) \tag{18}$$

The respective unit depends on the reaction order n_r, which in turn defines the unit of the pre-exponential coefficient A_r. The parameter E_a represents the activation energy. It is noted that the Westbrook and Dryer mechanism over-predicts the formulation of carbon monoxide [19]. The deviations are most noticeable for the two-step mechanism, which is also presented in [18]. Although the applied multistep mechanism reduces this trend, certain deviations in carbon monoxide mass fractions are still present.

3.3. Mesh Generation

The boundary conditions of the reference simulation and their respective walls are summarized in Figure 1. Besides the propellant specifications from Table 1, the injector and nozzle walls are modeled as isothermal walls considering friction and an ablative surface temperature of $T_w = 1000\ K$. Fuel pyrolysis is simplified by assuming a uniform effusive mass flux on the frictional fuel walls. On the nozzle exit, a supersonic boundary is set to allow for calculation of exit pressure instead of specifying a fixed ambient pressure.

In total, four different meshes were analyzed to ensure efficient simulation time without significant deviations due to the spatial resolution. A hybrid mesh structure with quadrilateral cells within the boundary layer and triangular cells in the field is used for each simulation case. The respective total numbers of cells are summarized in Table 3 with the starting mesh being referred to as R-1 and three refined meshes noted as R-2, R-3 and R-4.

3.4. Convergence Study

The simulation results show generally high agreement as can be seen in Figure 2(a). Here, the oxygen mass fraction is plotted over nozzle exit radius as an example for the main variables used for further calculations. As expected, the meshes with a higher number of cells are showing spatial convergence, while especially the R-1 mesh shows significantly smaller mass fractions. Based on these simulations, the R-3 mesh was selected as a reference in the following simulations, showing negligible errors compared to the fine mesh (R-4) but higher accuracy compared to the coarser meshes (R-1 and R-2). Additionally, temporal influence was analyzed in the form of solver iterations using local time-stepping for faster convergence. The respective variables that are being used within this study tend to converge after three to four million iterations with a relative error of less than 1 % compared to the asymptotic

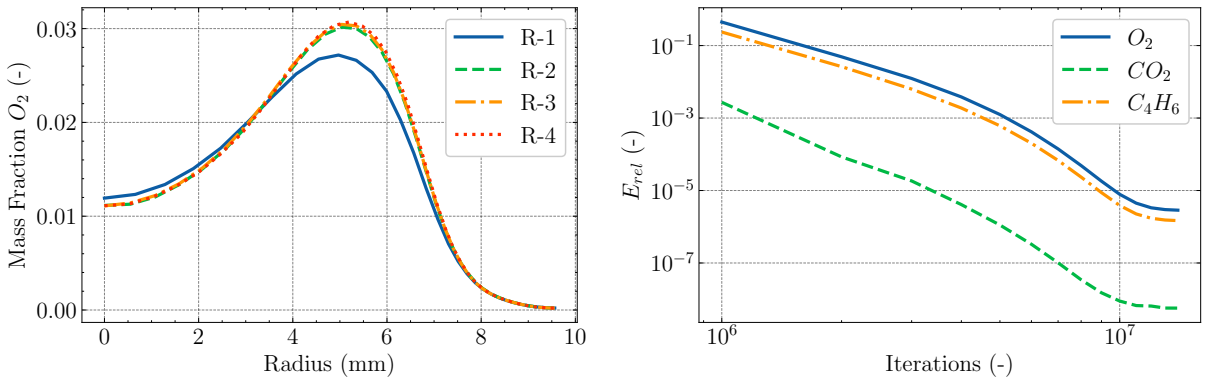

(a) Varying mesh resolution

(b) Temporal convergence (case R-3)

Fig 2. Convergence behaviour of selected mass fractions

Table 4. Summary of numerical results for different post-combustion chambers (PCC)

	Case	$L_{pcc}(mm)$	c^* (m/s)	F (N)	η_c (%)
Reference	R-3	13.0	1577.54	191.77	77.49
Menter-SST	T-1	13.0	1574.23	188.28	77.52
Shorter PCC	S-1	10.0	1576.49	191.57	77.14
	S-2	7.0	1575.89	190.46	76.66
	S-3	4.0	1575.24	190.37	76.21
Shorter PCC without turbulator plate	S-4	13.0	1572.24	186.44	71.39
	S-5	10.0	1571.56	186.00	70.98
	S-6	7.0	1570.92	185.50	70.63
	S-7	4.0	1570.23	184.92	70.21

value. More sensible values, e.g. heat fluxes, may still vary in certain ranges, but do not affect overall mass fractions as can be seen in Figure 2(b). Here, the root-mean-square error is calculated for the reference mesh R-3 at nozzle exit, which is where most of the values are evaluated.

4. Results

A representative temperature field of the R-3 domain is shown in Figure 3(a). Two flame zones resulting from the telescope fuel geometry are clearly visible within the combustion chamber. Downstream, the mixing of the flow advances resulting in a more uniform temperature field before decreasing due to nozzle expansion. The turbulator plate causes two large vortices and respective counter-vortices towards the chamber edges, visible in Figure 3(b). Although the two-dimensional representation does not account for three-dimensional mixing, the turbulator plate influences the cross-sectional flow field significantly. An overview for all simulation cases and their respective chamber length, characteristic velocity, thrust according to Equation 13 and combustion efficiency according to Equation 9 is summarized in Table 4. As mentioned above, R-3 refers to the reference case. The cases applying shorter post-combustion chambers are referred to as S-1, S-2 and S-3 ranging from 10 to 4 mm, in descending order. The complete length range (13 to 4 mm) was used in simulations without a turbulator plate downstream of the combustion chamber noted as S-4 to S-7. Finally, the reference mesh simulated with a two-equation turbulence model is referred to as T-1. The cases with the longest and shortest post-combustion chamber are illustrated in Figure 4.

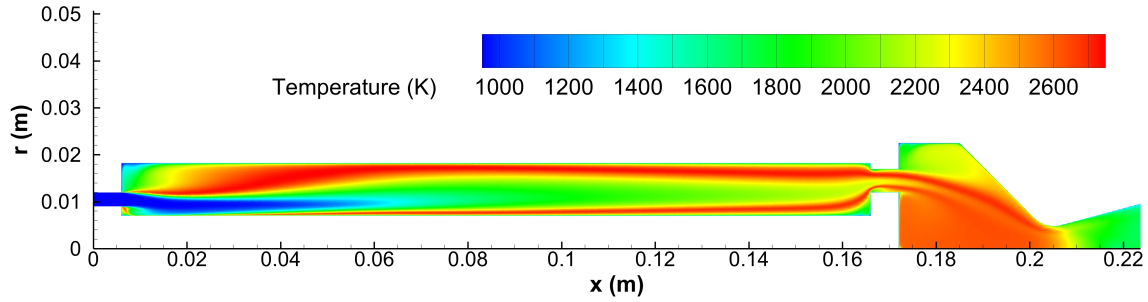

(a) Temperature field of the reference case (R-3)

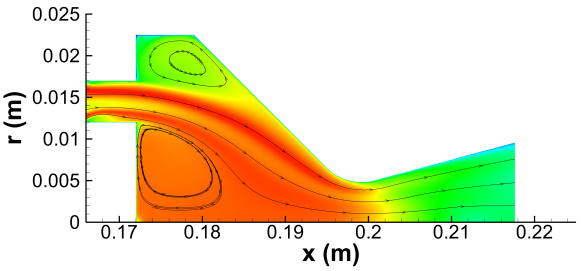

(b) Temperature field of a shorter chamber (S-2)

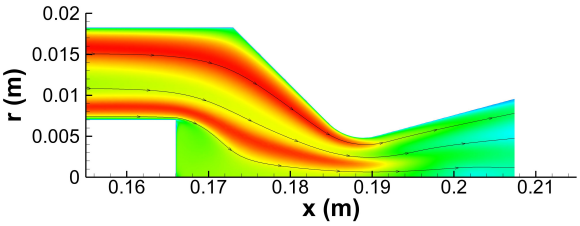

(c) Temperature field without a turbulator plate (S-7)

Fig 3. Comparison of post-combustion chamber designs

4.1. Varying Post-Combustion Chamber Length

Varying post-combustion chambers are shown in Figure 3 with different lengths for the reference case and the S-2 case as well as a post-combustion chamber without a turbulator plate, noted as case S-7. Temperature fields within the chambers are relatively similar, except for the case S-7. Here, both flame zones are less mixed than in the previous cases, causing the flame zones to be clearly distinguished downstream of the nozzle throat. This in return leads to a reduced mixing and therefore combustion efficiency. As expected, the carbon dioxide distribution within the flow field of the cases R-3, S-3, S-4 and S-7 correlates with the temperature fields. The respective mass fractions at nozzle exit are shown in Figure 5. Generally, oxidizer mass fractions increase and combustion products decrease with shorter chamber lengths. The large differences in the S-7 case support the significant influence of the turbulator plate. The insufficient mixing of the propellants is directly visible in the oxygen and 1,3-butadiene mass fractions. While the core stream is apparent in each simulated case, which is partly due to the axisymmetric definition of the simulation domain, it is mostly distinct in the cases S-4 to S-7. According to this, the fuel mass fractions illustrated in Figure 5(c) show higher values outside the core stream. The same behavior can be seen at the combustion end products, namely H_2O and CO_2, which are significantly lower compared to the cases S-1, S-2 and S-3.

The effect of varying post-combustion chamber length on the combustion efficiency η_c is illustrated in Figure 6(a). Here, the definition from Equation 9 was used to evaluate the combustion via steady-state mass fractions. The increase in efficiency shows linear behavior within the analyzed length between 0.13 and 0.14 %/mm. Hence, the direct effect of chamber length only represents a small enhancement for the combustion process. In contrast to this, the cases inhabiting a turbulator plate show a significant increase in efficiency of over 6 %. The same behavior was shown to be present for the actual engine thrust given in Figure 6(b). Considering the fact that the axisymmetric model of the simulation domain cannot properly display the turbulator plate, the effect is assumed to be even higher in real engines. Generally, these turbulator plates are designed with a specified number of ports, aligned circumferential on the cross-section between combustion and post-combustion chamber. The size of the ports is

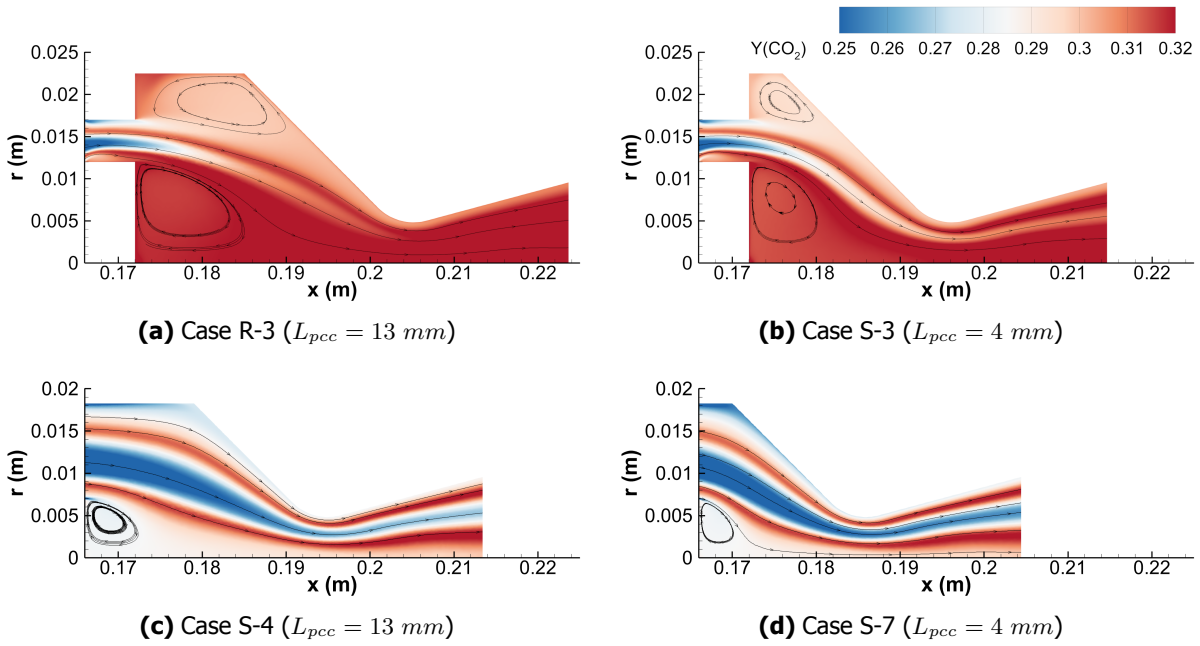

(a) Case R-3 ($L_{pcc} = 13\ mm$)

(b) Case S-3 ($L_{pcc} = 4\ mm$)

(c) Case S-4 ($L_{pcc} = 13\ mm$)

(d) Case S-7 ($L_{pcc} = 4\ mm$)

Fig 4. Carbon dioxide field solutions of the cases with the longest and shortest post-combustion chamber

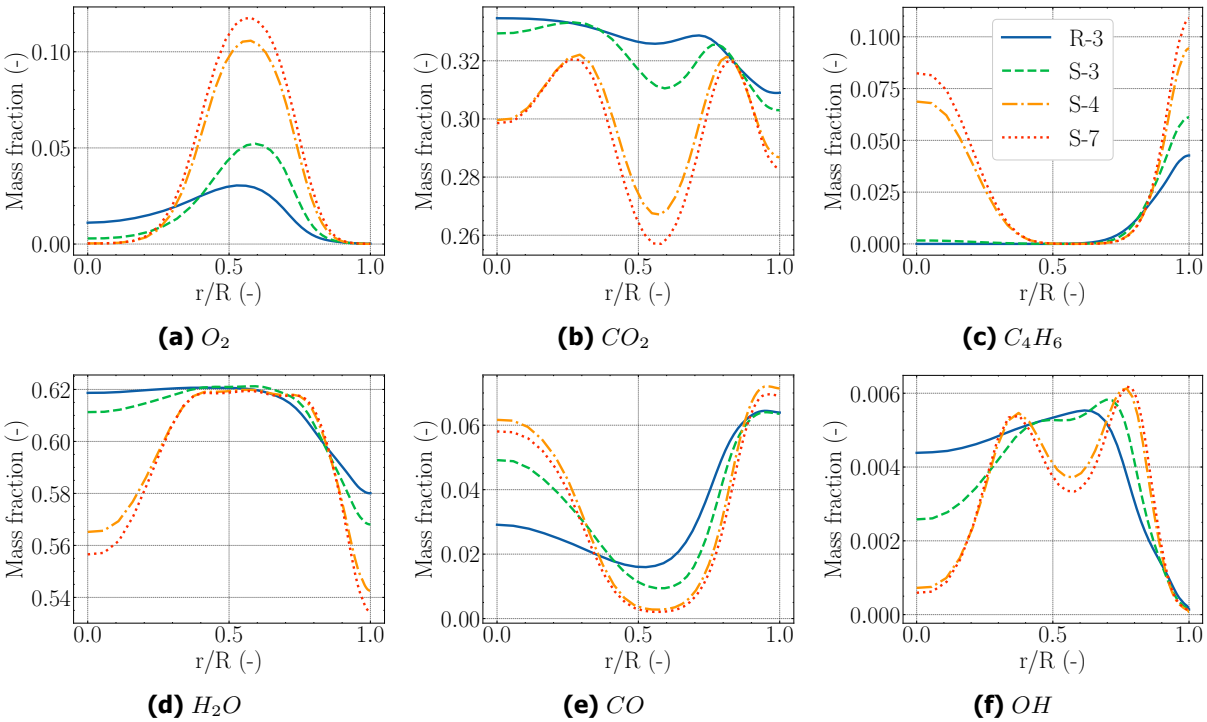

(a) O_2 **(b)** CO_2 **(c)** C_4H_6

(d) H_2O **(e)** CO **(f)** OH

Fig 5. Nozzle exit mass fractions in different post-combustion chambers

designed to not choke the flow crossing the turbulator section. Thus, the flow is strongly redirected and more vortices appear within the post-combustion chamber resulting in increased mixing. This effect cannot be fully described by axisymmetric simulations.

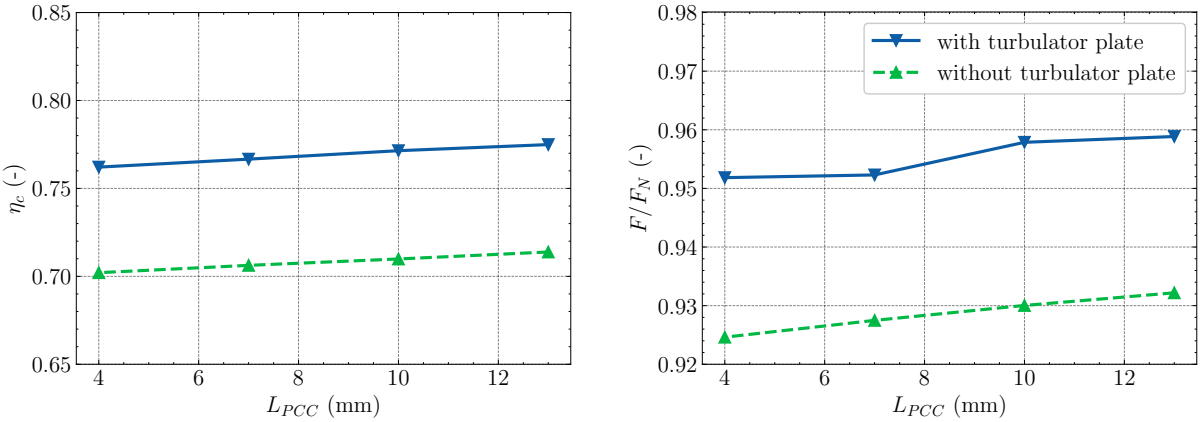

(a) Combustion efficiency

(b) Calculated thrust to nominal thrust ratio

Fig 6. Comparison of different post-combustion chamber lengths with and without a turbulator plate

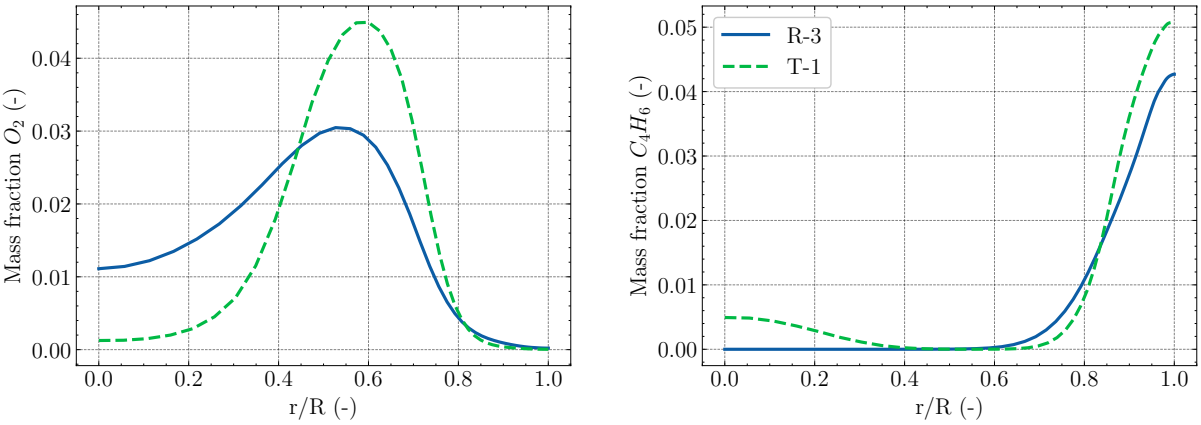

Fig 7. Oxidizer and fuel mass fractions at nozzle exit of reference mesh with one- (R-3) and two-equation (T-1) turbulence model

4.2. Turbulence Modeling Influence

As mentioned within section 3.2, the reference test case was also simulated using a two-equation turbulence model noted as case T-1. The results are compared in Figure 7. Here, oxidizer and fuel mass fractions at nozzle exit are plotted over the nozzle exit radius. While the flow fields are generally similar, small deviations appear, which are a result of different vortex sizes and flow paths. Considering the composition at nozzle exit, the core flow is more distinct than that of the reference case. However, this does not lead to less mixing or combustion, since the overall efficiency given in Table 4 is slightly higher with the two-equation model. The combustion efficiency is therefore not significantly influenced by the choice of the two turbulence models in the case of the present axisymmetric simulations. Nonetheless, the influence must be analyzed within three-dimensional simulations, where the flow field within the post-combustion chamber is assumed to be more turbulent.

5. Conclusion

Different definitions of combustion efficiencies are always based on energy conversion from chemical towards kinetic energy. Nonetheless, the calculation procedures vary depending on the focus of each study and its available data. The commonly used efficiency of the characteristic velocity was shown to

be less suited for numerical studies, since its main definition is based on global engine values. Therefore, a spatially resolved c^* field can be reduced to a scaled pressure field. A detailed analysis of the reactive flow was conducted using the gas composition, especially carbonaceous species, to obtain detailed insights into the effect of chamber design. The results presented above offer a qualitative overview of the post-combustion chamber length impact on combustion efficiency. The chamber length was shown to have only a limited influence on the combustion efficiency. In contrast to this, η_c strongly depends on the turbulator plate, which separates the combustion chamber and post-combustion chamber. It is noted that the applied reaction rate mechanism tends to overestimate the presence of carbon monoxide. This is the main reason why the compared efficiencies with a range of 70 % to 78 % are below common combustion efficiencies. In the definition of Equation 9, the carbon monoxide in the flow exiting the nozzle counts as unburnt and does not contribute to the combustion efficiency. A quantitative analysis of a propulsion system should therefore be conducted with a more detailed or adapted reaction rate mechanism. Also, the more complex turbulence field of three-dimensional flows must be considered to evaluate relevant fuel geometries and to optimize the systems weight.

References

[1] Božić, O., Porrmann, D., Lancelle, D., Hartwig, A.: Program AHRES and its Contribution to Assess Features and Current Limitations of Hybrid Rocket Propulsion. Proceedings of the 63rd Congress of International Astronautical Federation, IAC-12-C4, 1–5 October 2012, Naples, Italy

[2] Schwamborn, D., Gerhold, T., and Heinrich, R.: The DLR TAU-Code: Recent Applications in Research and Industry. ECCOMAS CFD 2006, 5–8 September 2006, Eggmond aan Zee, Netherlands

[3] Glaser, C., Hijlkema, J., Anthoine, J.: Bridging the Technology Gap: Strategies for Hybrid Rocket Engines. Aerospace 2023, 10, 901. https://doi.org/10.3390/aerospace10100901

[4] Lee, J., Moon, H., Kim, J.: Thermal–Combustion Coupled Instability in Hybrid Rockets with Fuel Blowing. Journal of Propulsion and Power 2023, Vol. 39, No. 3

[5] Tian, H., Jiang, X., Lu, Y., Liang, Y., Zhu, H., Cai, G.: Numerical Investigation on Hybrid Rocket Motors with Star-Segmented Rotation Grain. Aerospace 2022, 9, 585. https://doi.org/10.3390/aerospace9100585

[6] Glaser, C., Hijlkema, J., Anthoine, J.: Evaluation of Regression Rate Enhancing Concepts and Techniques for Hybrid Rocket Engines. Aerotecnica Missili Spazio 2022, 101, 267–292. https://doi.org/10.1007/s42496-022-00119-4

[7] Karabeyoglu, M. A., De Zilwa, S., Cantwell, B., Zilliac G.: Modeling of Hybrid Rocket Low Frequency Instabilities. Journal of Propulsion and Power 2005, Vol. 21, No. 6

[8] Bendana, F. A., Sanders, I.C., Stacy, N. G., Spearrin, R. M.: Localized Characteristic Velocity (c*) for Rocket Combustion Analysis Based on Gas Temperature and Composition Via Laser Absorption Spectroscopy Measurement Science and Technology, 32, 125203. https://doi.org/10.1088/1361-6501/ac18d3

[9] Rust, B., Gerlinger, P., Aigner, M.: An Improved Lobed Strut Injector Concept for Supersonic Combustion. 46th AIAA/ASME/SAE/ASEE Joint Propulsion Conference & Exhibit, 25–28 July 2010 Nashville, TN. https://doi.org/10.2514/6.2010-6962

[10] Castiñeira, D., Edgar, T. F.: CFD for Simulation of Steam-Assisted and Air-Assisted Flare Combustion Systems. Energy and Fuels 2006, 20, 1044–1056. https://doi.org/10.1021/ef050332v

[11] May, S., Božić, O.: Numerical Simulation of the Flow and Combustion Inside the Reaction Chamber of the AHRES Hybrid Rocket Engine. In: Dillmann, A. et al.: Notes on Numerical Fluid Mechanics and Multidisciplinary Design 132 - New Results in Numerical and Experimental Fluid Mechanics X. Springer, 2016, ISBN: 978-3-319-27278-8

[12] Gordon, S., McBride, B. J.: Computer Program for Calculation of Complex Chemical Equilibrium Compositions and Applications. Part 1: Analysis. No. NAS 1.61, 1311

[13] Chiaverini, M. J.: Review of Solid-Fuel Regression Rate Behaviour in Classical and Nonclassical Hybrid Rocket Motors. In: Chiaverini, M. J. et al.: Fundamentals of Hybrid Rocket Combustion and Propulsion - Progress in Astronautics and Aeronautics. Vol. 328

[14] Chiaverini, M. J., Harting, G. C., Lu, Y.-C., Kenneth, K. K., Peretz, A., Jones, H. S., Wygle, B. S., Arves J. P.: Pyrolysis Behavior of Hybrid-Rocket Solid Fuels Under Rapid Heating Conditions. Journal of Propulsion and Power 1999, Vol. 15, No. 6

[15] Allmaras, S. R., Johnson, F. T., Spalart, P. R.: Modifications and Clarifications for the Implementation of the Spalart-Allmaras Turbulence Model. Seventh International Conference on Computational Fluid Dynamics (ICCFD7), 9–13 July 2012 Big Island, Hawaii

[16] Menter, F. R.: Two-Equation Eddy-Viscosity Turbulence Models for Engineering Applications. AIAA Journal 1994, 32(8):1598–1605

[17] Menter, F. R., Kuntz, M., Langtry, R.: Ten Years of Industrial Experience with the SST Turbulence Model. In Hanjalić, K., Nagano, Y., Tummers, M.: Turbulence, Heat and Mass Transfer 4, Conference Proceeding Series, pages 625–632, 2003

[18] Westbrook, C. K., Dryer, F. L.: Simplified Reaction Mechanisms for the Oxidation of Hydrocarbon Fuels in Flames. Combustion Science and Technology, 1981, Vol. 27, pages 31–43

[19] Andersen, J., Rasmussen, C. L., Giselsson, T., Glarborg, P.: Global Combustion Mechanisms for Use in CFD Modeling under Oxy-Fuel Conditions Energy & Fuels, 2009, Vol. 23, pages 1379–1389